Gasc, J., et al., 2022, Deep-focus earthquakes: From high-temperature experiments to cold slabs: Geology, v. 50, https://doi.org/10.1130/G50084.1

Supplemental Material

Deep Focus Earthquakes: From High Temperature Experiments to Cold Slabs

Julien Gasc*, Clémence Daigre, Arefeh Moarefvand, Damien Deldicque, Julien Fauconnier, Blandine Gardonio, Claudio Madonna, Pamela Burnley and Alexandre Schubnel

*gasc@geologie.ens.fr

This file includes:

MATERIALS AND METHODS

Starting Material and Sample Preparation

Germanium olivine (Ge-Olivine, Mg_2GeO_4) was synthesized from Mg and Ge oxide powders by repeatedly heating the powders together at 1300°C in a Pt crucible and mixing them in an agate mortar. Excess Ge oxide, with respect to the Ge-olivine stoichiometry, was used in order to insure the presence of ~ 10 vol. % of germanium pyroxene (Ge-Px, MgGeO3) in the resulting powder. The purpose of incorporating Ge-Px is to better image deformation microstructures in the recovered samples, which is difficult to achieve in single phase aggregates due to the lack of contrast. A large cylindrical sample (~ 2.5 cm in diameter and 5 cm long) of Ge-olivine was then sintered from this powder by Hot Isostatic Pressing (HIP) at the ETH of Zurich in a gas apparatus at 200 MPa and 1200°C for 9 hours. Griggs-sized, cylindrical samples of 4.4 mm in diameter by 10 mm in length were then cored in the HIP sample.

One of these cores was subsequently fully reacted to Ge-spinel (Mg_2GeO_4 with a modified spinel structure, similar to that of Mg_2SiO_4 ringwoodite) in the new-generation Griggs apparatus at ENS Paris under hydrostatic conditions at 1.5 GPa and 930°C for 6 hours. Two 2.5 mm long cylinders were then sawed from this Ge-spinel core and used in experiment, TF2F, where the Ge-olivine core was only 5 mm long and sandwiched between the Ge-spinel samples.

The texture of the starting material, i.e., the synthetic Ge-olivine sinter, and that of the recovered deformed samples was analyzed by Scanning Electronic Microscopy (SEM). Images in backscatter electron mode were collected on all samples and Electron Back Scatter Diffraction (EBSD) maps were collected on the starting material (i.e., the HIP sample). The former allows detailed imaging of deformation microstructures as all three phases present in the recovered samples appear in different shades of gray thanks to their different densities and the latter allows precise characterization of grain size and aspect ratio, phase distribution and crystallographic preferred orientation (CPO). EBSD maps were processed with the help of the MTEX toolbox (Bachmann et al., 2010; Mainprice et al., 2015). Figure S*1* shows results from an EBSD map analysis, where grain boundaries were assigned with MTEX, thus allowing to visualize grain size and phase distribution. The average Ge-olivine grain size is about ~30 µm. Ge-pyroxene grains are evenly distributed within the Ge-olivine matrix and amount to 6 vol% (Figure S*1*a). Most Ge-olivine grains have a tabular shape and are slightly elongated (Figure S*1*b). This typical orthorhombic habitus of olivine usually associates the crystallographic *b*-axis with the shortest dimension of the grains (Miyazaki et al., 2013). Consequently, any shape preferred orientation of the grains induces a CPO of Ge-olivine, which is the case here during compaction of the powder in the canister used for HIP sintering, as the short axis of the grains and therefore the *b*-axis tend to align parallel to the compaction direction (Gasc et al., 2019). This results in slight a CPO dominated by a point maximum of the *b*-axis in the pole figures and an *a*-axis girdle (Figure S*1*c and d).

Deformation Experiments in the New Generation Griggs Rig

High pressure and temperature deformation experiments were performed in a new-generation Griggs type apparatus (Precigout et al., 2018). Full details regarding the whole experimental setup, including acoustics, are available in Moarefvand et al. (2021). The cored samples were encapsulated in Au sleeves closed on both ends with Au disks. The pressure medium consisted in solid NaCl. Resistive heating was generated through a graphite furnace and temperature was monitored with two K-type thermocouples.

Some Pb was used between the top of the sample and the alumina piston to cushion the sample during pressurization.

All experiments were performed at a constant pressure of 1.5 GPa and constant temperatures ranging between 506 and 843°C, i.e., in the Ge-spinel field. Temperature was ramped to the desired value during compression. The values read on the thermocouples were comprised between 540 and 900°C. However, these values represent an upper bound value, as both thermocouples are positioned closer to the graphite furnace than the sample is. Additional temperature calibration experiments were performed with one of the two thermocouples placed at the center of the cell, where the sample sits during deformation experiments. These calibrations indicate that the difference between the center of the cell and the thermocouple reading can be as high ~ 13 %, which therefore represents a lower bound for the actual mean sample temperature. These uncertainties represent a few tens of degrees and have been reflected on the reported temperatures which were corrected by 6.8 % from the initial thermocouple reading. This is also reported in table 1.

After reaching high P-T conditions, the deformation piston was moved by the hydraulic ram using a constant oil flow, which eventually translates to a steady displacement of the piston and a constant strain rate. Axial shortening (i.e., pure shear) was performed at strain rates ranging from 5.0×10^{-6} to 4.3×10^{-5} s^{-1}.

Mechanical Data Processing

Hit points were determined using a traditional approach, by identifying the intersection between the linear parts of the load-displacement curves corresponding to the run-in (i.e., when the deformation piston is moving through the lead piece) and the elastic loading of the sample (Holyoke and Kronenberg, 2010). The alumina piston used to deform the sample has a diameter of 5 mm, whereas the initial diameter of the sample is ~ 4.4 mm. However, due to sample barreling, the sample diameter increases upon axial strain. Therefore, stress was calculated using a surface correction assuming the sample kept a cylindrical shape and a constant volume during axial shortening. The actual surface on which the load of the piston is transmitted thus increases during deformation. It was assumed that this surface cannot exceed a value corresponding to the 5 mm diameter of the piston that transmits the axial load applied.

Acoustic Emissions Monitoring

The new generation Griggs rig at ENS is equipped with acoustic emission recording capability. Acoustic Emissions (AEs) were detected with the use of an Olympus® V156 transducer, which has a center frequency of 5 MHz and is polarized for shear wave detection. The transducer was glued under the carbide base plate located under the sample assembly during the experiment. It was glued with epoxy on an alumina disc to isolate it electrically from the press. The signal was amplified at 30 dB and filtered with a low-pass filter, which substantially improves the signal/noise ratio and therefore allows detecting smaller AEs. A threshold level was set above the background noise level in order to trigger AE recording. Waveforms of 8192 data points were collected with a sampling frequency of 50 MHz (i.e., the waveforms are 163.84 µs long) whenever the signal rose above the threshold level. In addition the unamplified and unfiltered signal was also recorded for all AEs. For small AEs, this raw recording does not provide useful information as the signal lies below noise level. For the largest AEs however, for which the amplified signal is saturated, the

unamplified signal is not and allows comparing the magnitude of these large events with much smaller ones.

Magnitude-Frequency Distributions

The relative amounts of energy radiated by the AEs were assessed by calculating the root mean square (RMS) of the signal for each AE. Arbitrary moment magnitudes, M_w, were then assigned to the AEs based on the RMS values, which scale proportionally with the amount of radiated energy, E_R, of each AE, i.e., RMS $\propto E_R \propto 10^{Mw}$ (Sammonds et al., 1992). The same trigger level was used in all experiments, which implies that the smallest detected events (right above the noise level) have the same magnitude in all experiments (– 8.6); with the exception of TF2F for which the smallest events are larger due to a lesser sensitivity of the transducer. These magnitudes were then used to investigate the magnitude-frequency distribution of the AEs using the conventional Gutenberg-Richter formalism, in which the number of events, *N,* of magnitude $\geq M_w$ obeys $\log_{10}(N) = a - b \times M_w$ (Gutenberg and Richter, 1949). Thanks to the fractal nature of fault networks, this relation holds from sample- to Nature-sized faults, as attested by the similar *b*-values obtained in experiments and seismology. Therefore the analysis of *b*-values yields precious information regarding the mechanisms in the samples that can be up-scaled and are relevant to DFEs in subduction zones The *b*-values were retrieved from a maximum likelihood estimate (Aki, 1965).

Frequency vs magnitude histograms are shown in Figure S3. Experiments BR1F and DU2S, for which seven and no AEs were collected, respectively, do not appear on this figure. Moment magnitude is defined as $M_w \propto {}^{2}/_{3} \log_{10}(L^n)$, where *L* is the length of the fault plane (Aki, 1981). Therefore, under constant *n*, *b*-values reflect the fractal dimension of earthquakes, or in the present case, AEs. This fractal dimension, D_H, is partly controlled by the topological dimension of the region where faults propagate, whether it be earthquakes or AEs. Under the standard assumption that $n = 3$, $D_H = 2b$ and the fractal dimension of AEs at 703°C, corresponding to a *b*-value of ~ 0.7 is $D_H = 1.4$ (Hirata, 1989; Legrand, 2002; Zhan, 2017). Whereas for DU1F at 843°C, $D_H = 3$. The value of $b = 1.1$ retrieved for BR2S at 609°C, has a greater uncertainty due to a lower number of AEs, however, it is consistent with the standard brittle failure observed in the mechanical data (Figure *1*). These data show a kink at $M_w \sim 7.6$ in the Gutenberg-Richter relationship, which may be attributed either to a higher completion magnitude than for other experiments or to a shift in *b*-value during deformation (Riviere et al., 2018).

Sample Recovering and Imaging

All deformed samples were recovered within their Au jacket and cut parallel to the shortening direction. Whenever a clear fault offset could be observed through the gold jacket, the cut was performed perpendicular to the apparent fault. These cross sections were mirror-polished by repeatedly polishing the surface with decreasing grit sizes down to colloidal silica (50 nm grain size). The samples were then analyzed by SEM so that the AEs obtained during deformation could be related to reaction progress and deformation microstructures. Images were collected in backscattered electron mode to benefit from the density contrast between Ge-px, Ge-spinel and Ge-olivine.

Growth Rates and Kinetics of The Olivine-Ringwoodite Transformation

The transformational faulting window identified in Figure 3 is centered on experiments performed at 703°C in the present study. We note that the BR2S data point (609°C) at a growth rate of 2×10^{-11} m s^{-1} corresponds to a few AEs and very limited ductility, which suggests that it lies close to the lower temperature limit of the brittle field. Similarly, the DU1F data point (843°C) at 2.2×10^{-8} m s^{-1}, which, despite the absence of brittle failure generated a large number of AEs, lies close to the upper temperature boundary. The temperature shift of this transformational faulting window between the present results and the ones previously reported is related to the kinetics of the olivine-ringwoodite transformation. In the present work, it is assumed that the reaction kinetic is primarily controlled by growth (and not nucleation) rate of the reaction products. Grain growth, $\dot{\chi}$ in m s^{-1}, is assumed to have the classic temperature dependence:

$$\ln(\dot{\chi}) = \ln(k_0) - \frac{E_a}{RT} + ln\left\{T\left[1 - exp\left(\frac{\Delta G}{RT}\right)\right]\right\} \qquad \text{(S1)}$$

, where k_0 is a kinetic constant, E_a is the activation energy in kJ mol^{-1}, R is the universal gas constant in kJ mol^{-1} K^{-1} and ΔG in kJ mol^{-1} is the Gibbs free energy change of the reaction at given PT conditions (Perrillat et al., 2016).

According to measured grain sizes on the recovered samples, experiments TF1F and TF3S (703°C) yield growth rates of 2-4 $\times 10^{-10}$ m s^{-1}. Experiment BR2S (609°C) yields ~2×10^{-11} m s^{-1}. Experiment BR1F (506°C) has very little spinel and nucleation barrier might have prevented growth of Ge-spinel grains altogether for most of the experiment; growth rates could not be retrieved from this experiment. For experiments TF3S (703°C), and DU1F and DU2S (843°C) high temperature and/or long durations resulted in high reaction extent. Consequently, grain growth impingement results in underestimating growth rates from final grain sizes. Therefore, growth rates were estimated based on measurements of grain sizes on images of TF1F, TF2F and TF3S and effects of temperature according the growth rate law of Burnley 1995 (Burnley, 1995) were used to estimate growth rates for other experiments (i.e., DU1F, BR2S, BR1F and DU2S), based on these measurements.

Growth rates for forsterite and fayalite in Figure 3a were calculated using equation (S1) according to Perrillat et al. (2016). The grain growth law reported by Burnley 1995, obtained using similar experiments in a Griggs device (Burnley, 1995) was used for former germanate studies. It was also used to convert the present grain growth values (obtained from measurements on recovered samples) to temperature. We note that this approach predicts larger temperatures than those estimated for our experiments, which implies that the growth rates retrieved are larger than expected from the growth rate law of (Burnley, 1995). This may be explained by a higher water content in our starting material, which was sintered at lower temperature (1200°C) than that of Burnley 1995 (1400°C). Gibbs free energy values, ΔG, of 2 and 4 kJ mol^{-1} were used for the silicate and germanate systems, respectively. They correspond to equilibrium oversteps of ~0.5 and 1 GPa for Forsterite and Ge-olivine, respectively.

Extrapolating to natural strain rates and temperatures, as is done in Figure 3b relies on the activation energy that describes the kinetic-temperature relationship. Experiments on the forsterite end-member had yielded 391 kJ mol^{-1} (Kubo et al., 2004). However, more recent data on olivine-ringwoodite kinetics have reported lower E_a values of 199-237 kJ mol^{-1} for silicate olivines with various Fe-Mg ratios (Diedrich et al., 2009; Du Frane et al., 2013; Perrillat et al., 2016). These apparent discrepancies reflect the various chemistry, pressure, temperature and water content used in these studies, which leaves a great uncertainty

regarding the actual activation energy. Figure 3b shows the result of an extrapolation using a value of 250 kJ mol^{-1}, therefore considered to be a reasonable estimate. Converting $\log(\dot{\chi})$ to equivalent reciprocal temperatures with equation (S1) and plotting them against $\log(\dot{\varepsilon})$, yields:

$$\log(\dot{\varepsilon}) - 4 \cong \log(\dot{\chi}) \qquad \text{(S2)}$$

with a slope of 1 (Figure 3). The slope in the $\log(\dot{\varepsilon})$ vs 1/T plots in Figure 3 therefore reflects the activation energy of grain growth, E_a, since combining equations S1 and S2 gives $\log(\dot{\varepsilon}) \propto \log(\dot{\chi}) \propto {E_a}/{T}$.

Frictional melting and Fault Propagation in Ge-spinel

A detailed examination of the fault in sample TF2F showed that melt was produced on the fault plane in the Ge-olivine sample, as evidenced by the presence of stretches of fine-grained recrystallized material adjacent to the fault plane (Figure 2c and d). The recrystallization of melt products is expected due to the extremely high cooling rates needed to quench amorphous olivine or spinel glass (Richet et al. 1993). Higher magnification images reveal that these regions are composed of small euhedral Ge-olivine grains embedded in a denser matrix (Figure S4 f and g). This microstructure is ubiquitous throughout the whole fault gouge, including next the main fault plane where the pyroxene grains show sharp offsets. In this latter case, however, grain size is even smaller and at the resolution limit of the SEM. Although these features are visualized here in the plane of the image, they have a 3D nature. Since they present important grain size gradients, it is therefore likely that only one of them is intercepted here through its core, where grains are coarser. Ge-olivine grains are embedded in an even smaller grain-sized matrix, the size of which cannot be resolved by SEM (Figure S4g). The high brightness of this matrix in the BSE images suggests that it consists of Ge-pyroxene, consistently with the lower melting point of pyroxene and therefore its later crystallization from the melt and its smaller grain size.

In TF2F, the Ge-olivine sample was sandwiched by two Ge-spinel samples of the same diameter, in which the fault also propagated. The fault plane was also examined in the Ge-spinel region (Figure S4). Similarly, the fault is extremely sharp and displays several evidences of frictional melting. We note that this is in agreement with the straightness of the fault across the entire sample, which may reflect fast rupture speed, as expected under high pressure conditions, where mode I crack opening is hindered and thus unable to accommodate high fault tortuosity (Bouchon et al., 2010; Zhan et al., 2015).

Conman Simulations

Thermal structures of subduction zones were simulated with the use of Conman 3.0 © (King et al., 2020; King et al., 1990). Thermal profile and velocity of the incoming lithosphere were adjusted to obtain thermal parameters, ϕ = plate age at trench × convergence rate × sin(slab dip) representing the extreme cases of the Bolivia and Tonga subduction zones (Syracuse et al., 2010). Age plates of 100 and 45 My and velocities of 20 and 6 cm y^{-1} were used for the cases of Tonga and Bolivia, respectively.

Table S1. Experimental conditions and results.

Experiment	T (°C)	Duration (s)	Volume fraction of Ge-Spinel	Growth Rate (m s^{-1})	Peak Stress (GPa)	Strain Rate at Peak Stress (× 10^{-5} s^{-1})	Mechanical Behavior	Number of AEs	AEs Cumulated RMS (V)	b-value
DU1F	843	13844	0.8	2.2×10^{-8}	1.29	2.79	Ductile	586	1.12	1.5 (0.070)
DU2S	834	54953	0.95	1.7×10^{-8}	1.31	0.495	Ductile	0	0	NA
TF1F	703	9592	0.2	2.6×10^{-10} *	2.15	2.69	Faulting	147	4.55	0.52 (0.042)
TF2F	703	6230	0.05	3.6×10^{-10}	2.23	4.31	Faulting	64	2.00	0.77 (0.095)
TF3S	703	57462	0.2	3.1×10^{-11} *	2.43	0.602	Faulting	633	1.01	0.62 (0.024)
BR2S	609	25449	0.1	2.0×10^{-11} *	2.37	0.998	Faulting	32	1.33	1.1 (0.18)
BR1F	506	7777	0.01	3.8×10^{-14}	2.19	3.54	Faulting	7	0.33	NA

Error on temperature is estimated to be +/- 6.8 %, (see supplementary material on deformation experiments for details). Standard deviation on obtained b-values is given between parentheses.

* Values obtained from grain sizes on recovered samples, other growth rates were inferred from growth rate laws (see supplementary information on growth rates).

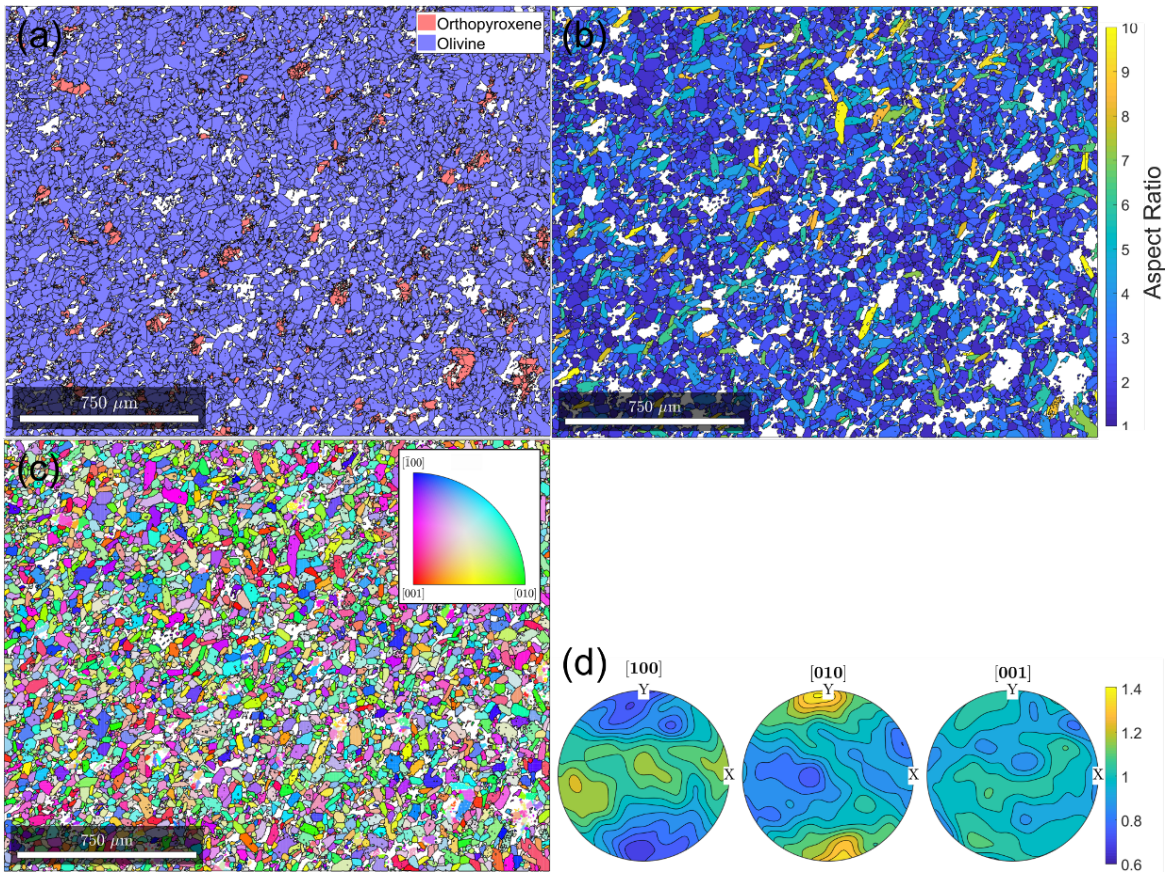

Fig. S1.

Results from EBSD data analysis. (a) Map showing phase distribution and grain boundaries (black contours) of Ge-pyroxene and Ge-Olivine. White represents unindexed pixels due to poor diffraction quality. (b) Ge-olivine grains color coded as a function of their aspect ratio. (c) Map showing the orientation of Ge-olivine grains with in the direction of the long axis of the cylinders used for the experiments (normal to the image plane). Grains are color-coded according to the inverse pole figure in the inset. (d) Pole figures showing the orientation of Ge-olivine grains with respect to the microscope reference frame. The pole figures were rotated 90° here so that the length of the cylinder (i.e., the shortening direction during deformation) is vertical. The color scale corresponds to multiples of average density of crystal axes. Densities were calculated using one point per grain to avoid overrepresentation by larger grains.

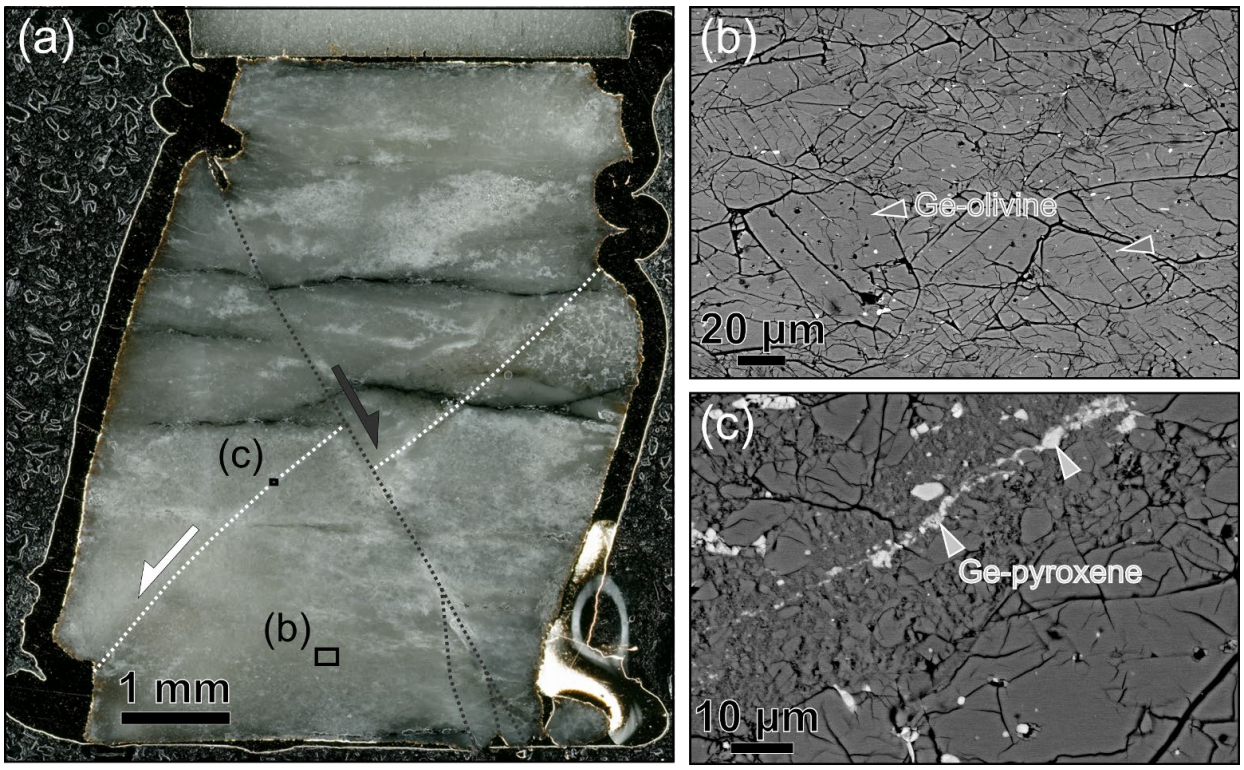

Fig. S2.

Microscopy images of sample BR1F. (a) Optical microscopy image showing the entire sample in its Au capsule. The dashed lines and half-headed arrows indicate the location and the slip direction of two conjugated faults that induced major offsets in the sample. (b) SEM image of the bulk of the sample according to the rectangle in (a). The homogeneous image contrast in BSE mode reveals the absence of Ge-spinel. The initial shape of Ge-olivine grains is still visible (arrow heads); they are heavily fragmented due to the relatively cold temperature of deformation. (c) SEM image of one of the faults according to the rectangle in (a). Shearing of Ge-pyroxene grains (brighter phase) shows the important strain localization that occurred over widths of 10-20 µm. The fault gouge displays a brecciated texture and, unlike for transformational faulting samples, does not contain Ge-spinel.

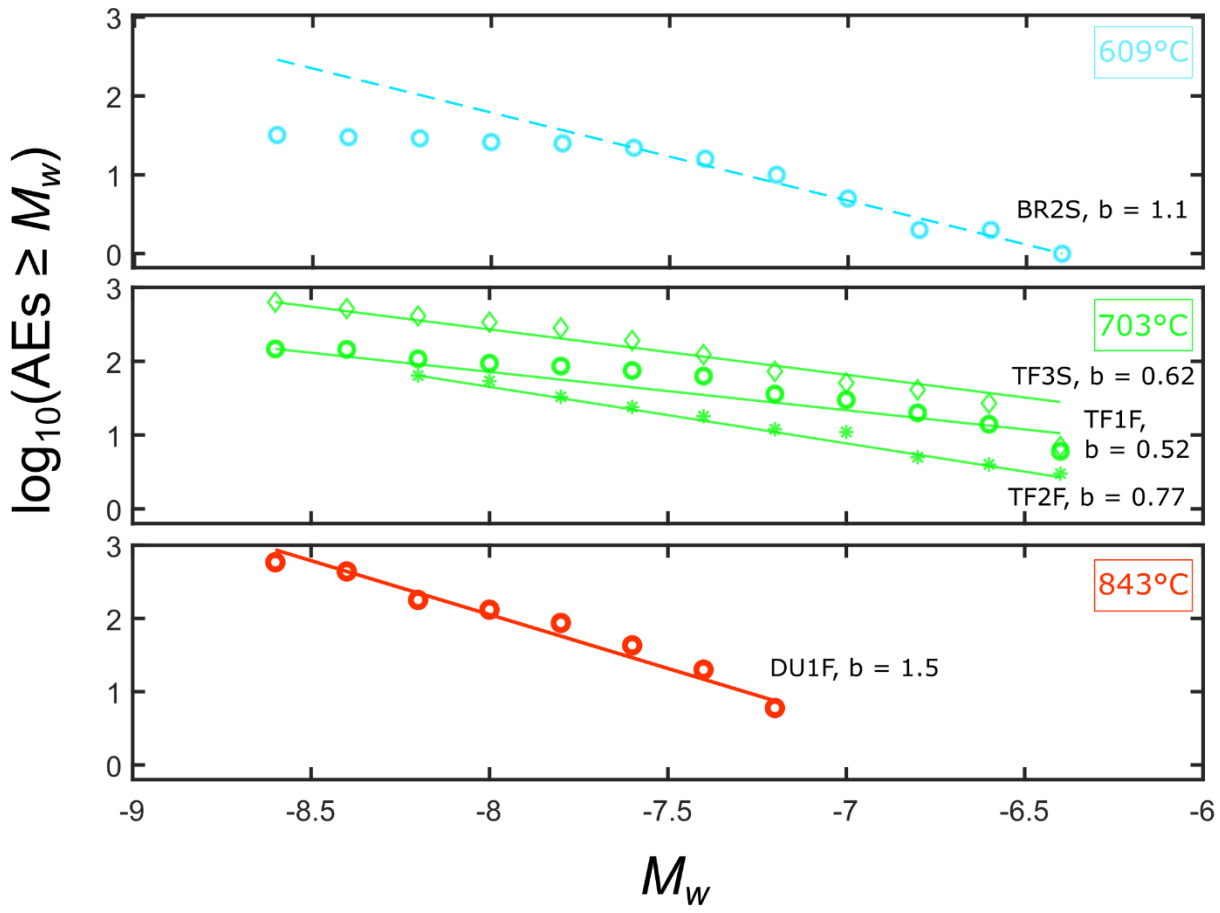

Fig. S3.

Magnitude frequency distribution of AEs and corresponding *b*-values. Experiment number and associated *b*-value are provided next to each dataset.

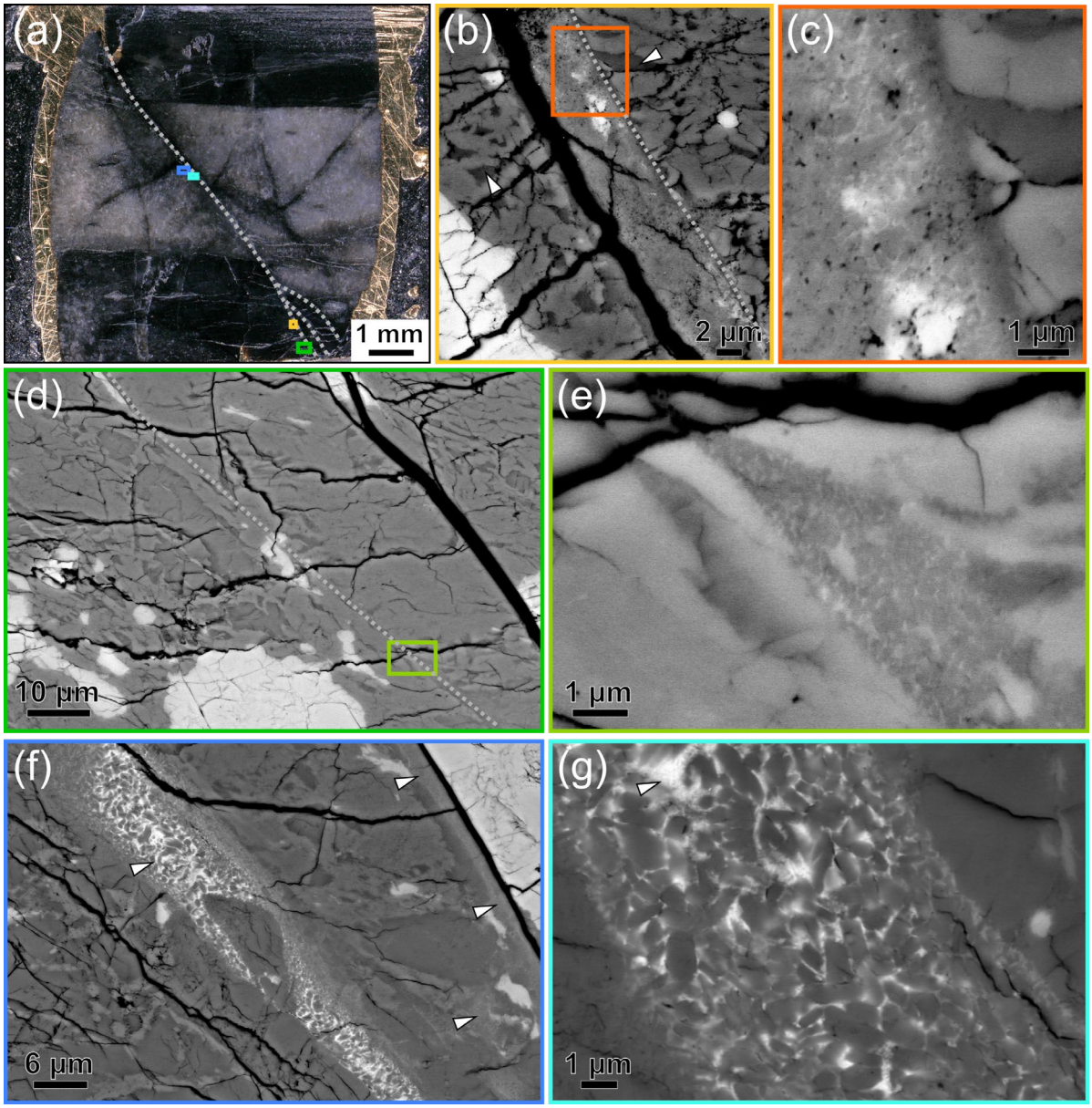

Fig. S4.

Microstructures of sample TF2F. (a) Optical image showing the whole sample. Ge-olivine appears brighter at the center, while the darker regions at the top and bottom of the sample correspond to Ge-spinel. The main fault (dashed lines) propagated through all three parts of the sample. (b)-(e) SEM images of the fault according to the rectangles in (a). (b) The fault, observed here in the bottom Ge-spinel bit, is a few microns wide. Arrow-heads point at remnant Ge-olivine grains. (c) The fault gauge contains an extremely fine-grained texture revealing static recrystallization, typical of quenched melts. (d) Here the fault plane (dashed line) is more discrete with no definable thickness. However, towards the bottom of the image, it widens and forms injectite type features. (e) At high magnification, this feature reveals the same quench texture observed in (c), indicative of frictional melting. (f) Shows a detailed view of the feature described in Figure 2, which reveals that the same quench texture is ubiquitous near the fault plane (arrow-heads) with a smaller grain size. (g) At higher magnification, submicron olivine grains are observed. These are embedded in a denser matrix, composed of nanometric Ge-pyroxene grains (arrow-head).

References

Aki, K., 1965, Maximum Likelihood Estimate of b in the Formula logN=a-bM and its Confidence Limits: Bulletin of the Earthquake Research Institute, v. 43, p. 237-239.

Aki, K., 1981, A Probabilistic Synthesis of Precursory Phenomena, Earthquake Prediction, p. 566-574.

Bachmann, F., Hielscher, R., and Schaeben, H., 2010, Texture Analysis with MTEX - Free and Open Source Software Toolbox: Texture and Anisotropy of Polycrystals Iii, v. 160, p. 63-+.

Bouchon, M., Karabulut, H., Bouin, M. P., Schmittbuhl, J., Vallee, M., Archuleta, R., Das, S., Renard, F., and Marsan, D., 2010, Faulting characteristics of supershear earthquakes: Tectonophysics, v. 493, no. 3-4, p. 244-253.

Burnley, P. C., 1995, The fate of olivine in subducting slabs: A reconnaissance study: American Mineralogist, v. 80, no. 11-12, p. 1293-1301.

Diedrich, T., Sharp, T. G., Leinenweber, K., and Holloway, J. R., 2009, The effect of small amounts of H2O on olivine to ringwoodite transformation growth rates and implications for subduction of metastable olivine: Chemical Geology, v. 262, no. 1-2, p. 87-99.

Du Frane, W. L., Sharp, T. G., Mosenfelder, J. L., and Leinenweber, K., 2013, Ringwoodite growth rates from olivine with similar to 75 ppmw H2O: Metastable olivine must be nearly anhydrous to exist in the mantle transition zone: Physics of the Earth and Planetary Interiors, v. 219, p. 1-10.

Gasc, J., Demouchy, S., Barou, F., Koizumi, S., and Cordier, P., 2019, Creep mechanisms in the lithospheric mantle inferred from deformation of iron-free forsterite aggregates at 900-1200 degrees C: Tectonophysics, v. 761, p. 16-30.

Gutenberg, B., and Richter, C., 1949, Seismicity of the earth and associated phenomena, Princeton, New Jersey.

Hirata, T., 1989, Fractal dimension of fault systems in japan - Fractal structure in rock fracture geometry at various scales: Pure and Applied Geophysics, v. 131, no. 1-2, p. 157-170.

Holyoke, C. W., and Kronenberg, A. K., 2010, Accurate differential stress measurement using the molten salt cell and solid salt assemblies in the Griggs apparatus with applications to strength, piezometers and rheology: Tectonophysics, v. 494, no. 1-2, p. 17-31.

King, S., Raefsky, A., and Hager, B. H., 2020, ConMan version 3.0.0, Zenodo.

King, S. D., Raefsky, A., and Hager, B. H., 1990, CONMAN - Vectorizing a finite-element code for incompressible 2-dimensional convection in the earths mantle: Physics of the Earth and Planetary Interiors, v. 59, no. 3, p. 195-207.

Kubo, T., Ohtani, E., and Funakoshi, K., 2004, Nucleation and growth kinetics of the alpha-beta transformation in Mg2SiO4 determined by in situ synchrotron powder X-ray diffraction: American Mineralogist, v. 89, no. 2-3, p. 285-293.

Legrand, D., 2002, Fractal dimensions of small, intermediate, and large earthquakes: Bulletin of the Seismological Society of America, v. 92, no. 8, p. 3318-3320.

Mainprice, D., Bachmann, F., Hielscher, R., and Schaeben, H., 2015, Descriptive tools for the analysis of texture projects with large datasets using MTEX: strength, symmetry and components: Rock Deformation from Field, Experiments and Theory: a Volume in Honour of Ernie Rutter, v. 409, p. 251-271.

Miyazaki, T., Sueyoshi, K., and Hiraga, T., 2013, Olivine crystals align during diffusion creep of Earth's upper mantle: Nature, v. 502, no. 7471, p. 321-+.

Moarefvand, A., Gasc, J., Fauconnier, J., Baïsset, M., Burdette, E., Labrousse, L., and Schubnel, A., 2021, A new generation Griggs apparatus with active acoustic monitoring: Tectonophysics, v. 816, p. 229032.

Perrillat, J. P., Chollet, M., Durand, S., van de Moortele, B., Chambat, F., Mezouar, M., and Daniel, I., 2016, Kinetics of the olivine-ringwoodite transformation and seismic attenuation in the Earth's mantle transition zone: Earth and Planetary Science Letters, v. 433, p. 360-369.

Precigout, J., Stunitz, H., Pinquier, Y., Champallier, R., and Schubnel, A., 2018, High-pressure, High-temperature Deformation Experiment Using the New Generation Griggs-type Apparatus: Jove-Journal of Visualized Experiments, no. 134.

Richet, P., Leclerc, F., and Benoist, L., 1993, Melting of forsterite and spinel, with implications for the glass-transition of mg2sio4 liquid: Geophysical Research Letters, v. 20, no. 16, p. 1675-1678.

Riviere, J., Lv, Z., Johnson, P. A., and Marone, C., 2018, Evolution of b-value during the seismic cycle: Insights from laboratory experiments on simulated faults: Earth and Planetary Science Letters, v. 482, p. 407-413.

Sammonds, P. R., Meredith, P. G., and Main, I. G., 1992, Role of pore fluids in the generation of seismic precursors to shear fracture: Nature, v. 359, no. 6392, p. 228-230.

Syracuse, E. M., van Keken, P. E., and Abers, G. A., 2010, The global range of subduction zone thermal models: Physics of the Earth and Planetary Interiors, v. 183, no. 1-2, p. 73-90.

Zhan, Z., Shearer, P. M., and Kanamori, H., 2015, Supershear rupture in the 24 May 2013 M-w 6.7 Okhotsk deep earthquake: Additional evidence from regional seismic stations: Geophysical Research Letters, v. 42, no. 19, p. 7941-7948.

Zhan, Z. W., 2017, Gutenberg-Richter law for deep earthquakes revisited: A dual-mechanism hypothesis: Earth and Planetary Science Letters, v. 461, p. 1-7.